Radiative Heating on the After-Body of Martian Entry Vehicles

A. M. Brandis,[*] D. A. Saunders,[†]

ERC Incorporated at NASA Ames Research Center, Moffett Field, CA, 94035, USA

C. O. Johnston,[*]

NASA Langley Research Center, Hampton, VA, 23669, USA

B. A. Cruden[†] T. R. White,[*]

ERC Incorporated at NASA Ames Research Center, Moffett Field, CA, 94035, USA

This paper presents simulations of the radiative heat flux imparted on the after-body of vehicles entering the Martian atmosphere. The radiation is dominated by CO_2 bands emitting in the mid-wave infrared spectral region. This mechanism has traditionally not been considered in the design of past Mars entry vehicles. However, with recent analysis showing that the CO_2 radiation can be greater than convective heating in the wake, and with several upcoming and proposed missions to Mars potentially affected, an investigation of the impact of this radiation is warranted. The focus of this paper is to provide a better understanding of the impact to aerothermal heating predictions and to provide comparisons between NASA's two main radiation codes, NEQAIR and HARA. The tangent slab approximation is shown to be overly conservative, by as much as 58%, for most back-shell body point locations compared to using a full angular integration method. However, due to the complexity of the wake flow, it is also shown that tangent slab does not always represent an upper limit for radiative heating. Furthermore, analysis in this paper shows that it is not possible to provide a general knock-down factor from the tangent slab results to those obtained using the more rigorous full integration method. When the radiative heating is accounted for on the after-body, the unmargined total heat flux can be as high as 14 W/cm^2.

I. Introduction

THE radiative component of heat flux on the after-body of vehicles entering the Martian atmosphere has traditionally been neglected. However, due to theoretical analyses,[1] simulations,[2,3,4,5,6] and experiments[7] highlighting that the mid-wave infrared CO_2 radiation can be significant, the impact to flight vehicles needs to be quantified. Understanding the magnitude of the radiation and corresponding uncertainties may influence future margin policies,[8] and hence the back-shell material selection and thickness. In this work, the magnitude of the radiative heat flux has been calculated on the after-body for two geometries from successful Mars missions. These same geometries are being flown on the upcoming InSight and Mars 2020 missions, and their heat shield sizings may be affected by this analysis. InSight is a 2016 Mars lander aimed at measuring the seismic activity on the planet's surface. The structural geometry is identical to Phoenix (70 deg sphere/cone, 2.65 m aeroshell diameter). However, InSight will utilize a faster entry than Phoenix (but slower than Pathfinder) at 6.3 km/s. The InSight entry is ballistic with a nominal angle of attack (AoA) of zero degrees. Mars 2020 will utilize the same geometry as the Mars Science Laboratory (MSL) which successfully landed on the surface of Mars in 2012. Mars 2020 will include the MEDLI2 instrumentation suite that will enable, among other things, the measurement of pressure and in-depth heating to the thermal protection system. The in-depth temperature measurements can be used to back out the heating encountered by the vehicle during entry. Analysis in this work includes a comparison of the flow-fields generated by the

---

[*]Research Scientist, Aerothermodynamics Branch, and Senior Member AIAA. Contact: aaron.m.brandis@nasa.gov
[†]Senior Research Scientist, Aerothermodynamics Branch, and Senior Member AIAA.

American Institute of Aeronautics and Astronautics

DPLR and LAURA computational fluid dynamics (CFD) codes and spectral comparisons between NASA's two main predictive radiation tools, NEQAIR and HARA. A previous analysis[9] showed that tangent slab was overly conservative for after-body radiation calculations for Earth entry, and this work will now examine cases relevant to Mars entry.

II.   Description of Predictive Codes

This section will briefly detail the flow-field and radiation codes used in the present analysis.

II.A.   LAURA

The Langley Aerothermodynamic Upwind Relaxation Algorithm (LAURA) is a high fidelity, structured grid flow solver, specialized for hypersonic re-entry physics, utilizing state-of-the-art algorithms for CFD simulations.[10,11] Key elements of LAURA include Roe's averaging[12] and Yee's Symmetric Total Variation Diminishing (STVD)[13] formulation of second-order, inviscid flux. Its non-equilibrium real-gas Navier-Stokes flow calculations are parallelized.

II.B.   DPLR

DPLR uses a finite-volume discretization to solve the reacting Navier-Stokes equations for fluids in thermo-chemical non-equilibrium on structured grids. It too is parallelized for efficient computing on large clusters. While the software was originally designed for steady-state aerothermodynamic analysis of planetary entry vehicles, DPLR has evolved over the years to include a broad spectrum of numerical and physical models that enable it to accurately simulate most compressible flows. Additional details on DPLR's capabilities can be found in the references 14, 15, 16.

II.C.   HARA

The High-temperature Aerothermodynamic RAdiation (HARA) model applied in the present study is discussed in detail by Johnston et al.[17,18] A line-by-line approach is used for atoms and optically thick molecules, while a smeared band model is used for optically thin molecules. HARA is based on a set of atomic levels and lines from the National Institute of Standards and Technology (NIST)[19] and Opacity Project databases.[20] The atomic bound-free model is composed of cross sections from the Opacity project's online TOPbase,[21] which were curve fit by Johnston.[17] HARA uses tangent slab as the default option for calculating the wall-directed radiative heat flux, with an option for running full angular integration for appropriate cases. Unless stated otherwise, results presented using HARA in this work are based on flow-fields generated by LAURA.

II.D.   NEQAIR

Non-EQuilibrium AIR (NEQAIR) is a line-by-line radiation code which computes spontaneous emission, absorption and stimulated emission due to transitions between various energy states of chemical species along a line-of-sight.[22] Individual electronic transitions are considered for atoms and molecules, with the molecular band systems being resolved for each rotational line. Since the report of Whiting et al.,[22] numerous updates have been incorporated into NEQAIR, such as: using the latest version of the NIST atomic database (version 5.0),[23] using the bound-free cross sections from TOPbase,[21] incorporating the CO_2 database from CDSD-4000,[1] parallelization and improvements to the mechanics of QSS. This latest version of NEQAIR is known as v14.0.[24] As with HARA, NEQAIR uses the tangent slab approximation as the default option for radiation transport. Furthermore, ancillary utilities enable NEQAIR to perform full angular integration calculations for appropriate cases. Unless stated otherwise, results presented using NEQAIR in this work are based on flow-fields generated by DPLR.

III.   Validation of Relevant Models

III.A. CO_2 Radiation

The Carbon Dioxide Spectroscopic Databank, CDSD-4000,[1] is the most extensive line list for CO_2 presently available. CDSD-4000 is intended to be capable of simulating CO_2 spectra at temperatures up to 5000 K.

American Institute of Aeronautics and Astronautics

The sheer number of lines in the database make their full inclusion in NEQAIR or HARA impractical, so different approaches have been taken to implement CDSD-4000 within the codes.

NEQAIR has incorporated a reduced form of the database by using a pseudo-continuum approach.[5] The NEQAIR CO_2 model contains 876,000 lines and covers all known CO_2 IR band systems, including the bands at 2.0, 2.7, and 4.3 μm. A series of high-temperature CO_2 radiation experimental test cases were identified to validate the NEQAIR CO_2 model.[5]

To maintain HARA's efficiency, which is particularly useful for the full angular integration computations required in the after-body, the CO_2 IR spectrum is tabulated for a range of temperatures and pressures externally from the code (the pressure dependence is required for line broadening above 0.1 atm). These tables, which are only computed once, are read and interpolated by HARA for actual shock layer radiation computations. Because only a single temperature is used when making the tables, it is assumed that the two (translational and vibrational) temperatures in the flow-field are nearly equilibrated, which is typically the case, even for the after-body. A total of 500,000 spectral points was found to provide sufficient line resolution for the range of temperatures and pressures considered, with weakly radiating regions such as 3350 - 4000 nm ignored.

Figure 1 shows a comparison of NEQAIR and HARA calculations, both based on the same DPLR flow-field, for a representative back-shell case. The figure shows that the spectral radiance is in very good agreement between the two codes, with the integrated values being within 3% of each other. The tangent slab evaluations were within 2%. Thus, any differences greater than a few percent between the two codes in the following sections are most likely due to differences in either the flow-field used or the angular integration methods.
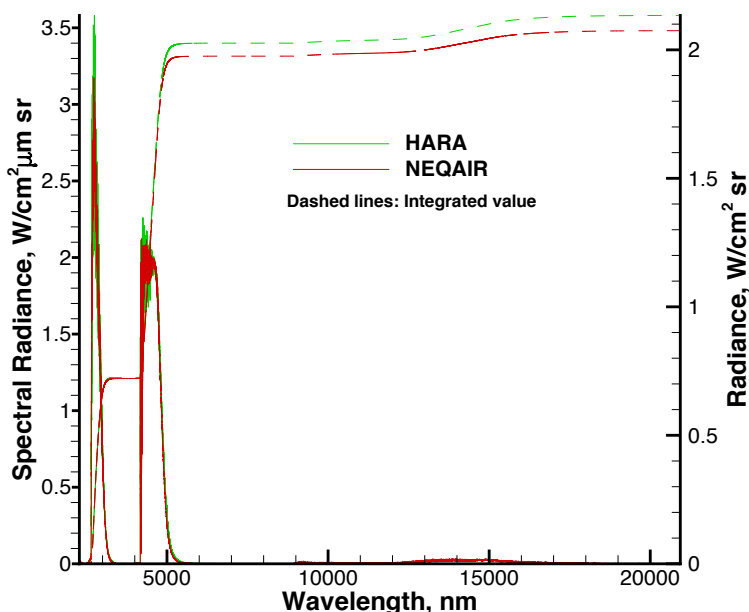

Figure 1. Comparison of CO_2 back-shell radiation between NEQAIR and HARA.

As CDSD-4000 contains such a large of number of lines and as the conditions relevant to Mars entry cause the radiation on the back-shell to be partially black body limited, care must be taken not to under-resolve the spectral grid. For example, the 4 μm band may initially appear to be black body limited (which would mean a sparse spectral grid would be acceptable), as shown in Fig. 2(a). However, as shown in higher resolution in Fig. 2(b), the spectrum regularly dips down from the black body limit, and capturing these departures from the black body is important for evaluating the total heat flux. These features are not apparent when the spectrum is smoothed or down-sampled, as in Fig. 1.
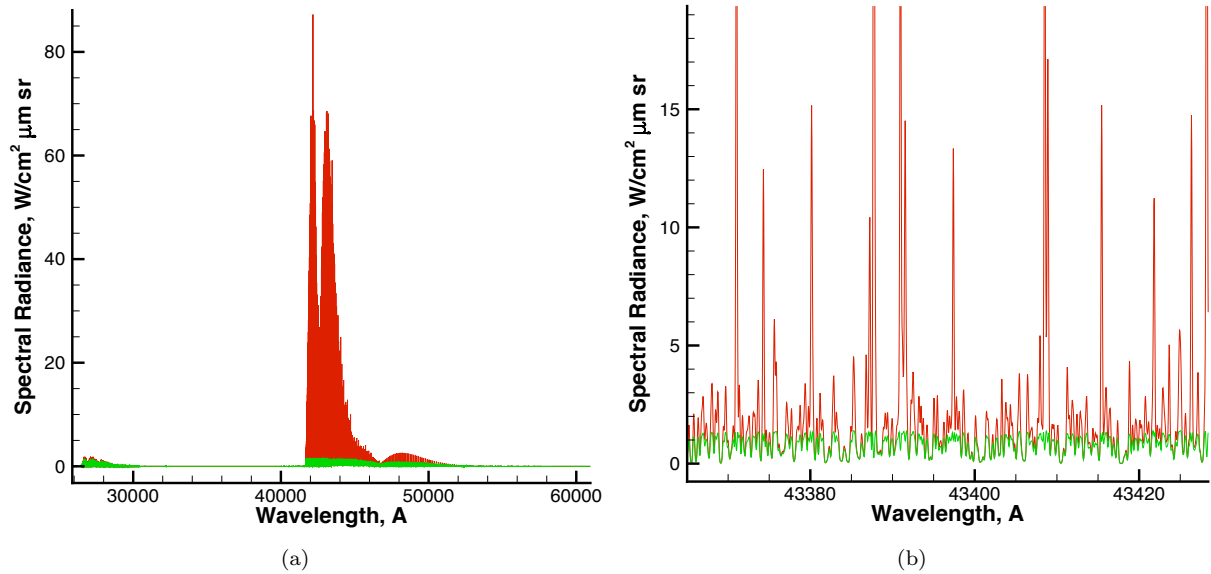
American Institute of Aeronautics and Astronautics

(a)

(b)

Figure 2. Spectral radiance highlighting the level of self-absorption for MWIR CO_2. Self-absorbed results shown in green, optically thin results shown in red.

III.B. Flow-field Comparisons

The results presented in this section are taken from representative solutions in the wake to highlight the differences between the two flow-fields calculated by DPLR and LAURA. Figure 3 shows the profiles of the translational temperature, vibrational temperature and the number densities of CO and CO_2 from LAURA and DPLR simulations of the same vehicle and trajectory point. LAURA predicts a higher temperature for most of the shock layer, while DPLR predicts a higher temperature close to the body. Furthermore, LAURA is predicting a larger concentration of CO_2 in the wake. These differences are due to the use of different reaction rates for the dissociation of CO_2 and CO and the different surface catalycity models implemented in the two codes.[25]
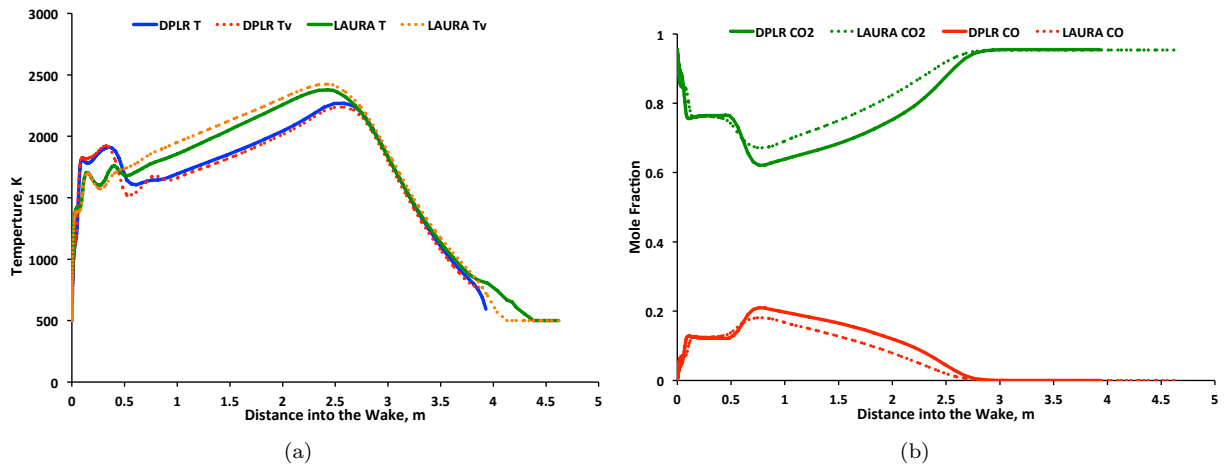

(a)

(b)

Figure 3. DPLR and LAURA results for (a) T, Tv and (b) mole fraction of CO and CO_2 for an InSight back-shell line of sight. A distance of 0 on the x-axis represents the body location.

III.C. Full Angular Integration

Due to the complexities of the flow found in the wake of a vehicle, and the more complicated geometries on the back shell, using a tangent slab approximation is questionable for after-body radiative heating calculations.[6] For more accurate estimation of radiative heat flux on the after-body, a full angular integration is required.

American Institute of Aeronautics and Astronautics

Full angular integration is achieved by conducting a numerical integration of radiance at a body point with respect to solid angle over all possible lines of sight to/from the body point. The method that has been implemented with DPLR, to prepare input data for NEQAIR, begins with the construction of a unit-radius spherical surface octant that is triangulated according to a specified number of points distributed uniformly along each edge. In general, four such octants, appropriately transformed, define the hemisphere surface (Fig. 4) that can be "seen" by the body point. Two octants commonly suffice when the body point is on the center line of an axisymmetric body. The hemisphere is centered at the body point and tangential to the surface, with the vertices of the combined octant triangulations defining the lines of sight to/from the body point. Note that triangulation provides a more uniformly distributed set of lines than does the use of discretized lines of latitude and longitude, but no triangulation of an octant surface can be truly uniform, since the elements must be right angle triangles at the three octant "corners" but they tend towards equilateral triangles elsewhere. Lines of sight within the flow solution volume grid are constructed by intersecting each 2-point line between body point and triangle vertex with the outer grid boundary. Finally, the required inputs to NEQAIR are evaluated using a multiblock volume grid form of the Alternating Digital Tree (ADT) search method,[26] which interpolates flow-field temperatures and species number densities onto the discretized hemisphere lines of sight. NEQAIR is scripted to run in "line of sight" mode (i.e., no tangent slab evaluation is made) on all of these lines. The normal component of radiance from all lines is then integrated with respect to solid angle to produce the more thorough estimate of radiative heat flux at the body point.
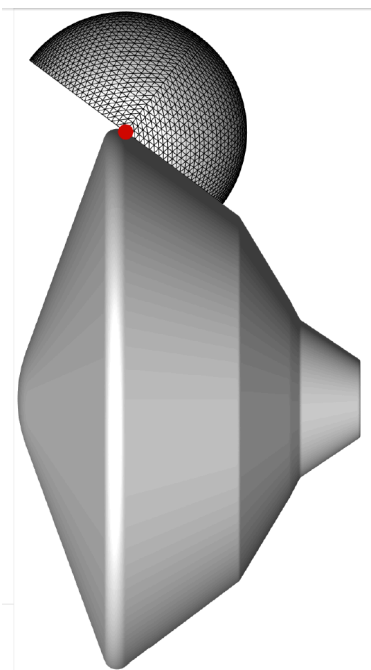

Figure 4. MSL geometry showing a unit-radius hemisphere triangulation used to generate lines of sight needed for full angular integration calculations.

A similar methodology for conducting full angular integration calculations has also been implemented with the LAURA code, to prepare input data for HARA. A brief summary of the implementation follows, and further details can be found in Mazaheri et al.[6] The LAURA full angular integration (referred to as "ray tracing" in Ref. 6) consists of a series of simple vector analyses followed by a searching algorithm that finds grid cells for which the lines of sight are passing through. It starts with constructing a series of lines of sight spanning the 3-D space from selected surface points outward and determining their intersections with volume grid cells. The flow-field solution is interpolated onto each of these lines of sight, and the corresponding spectral radiance is calculated with HARA. The integrated intensity along each of these lines at the selected surface points is then obtained, and the resultant total radiation incident to these surface points computed via integration with respect to solid angle.[6]

American Institute of Aeronautics and Astronautics

IV. Impact to Flight

IV.A. Phoenix Geometry

The Mars Phoenix spacecraft was launched on August 4th of 2007 and landed successfully on May 25th of 2008. Phoenix utilized a 70-degree half-angle sphere-cone rigid capsule fore-body geometry.[27] Similar shapes were also successfully used to land payloads for the Viking, Pathfinder and MER missions.[27] NASA's upcoming Discovery Program mission, InSight (due to be launched in March 2016), is based on the same sphere-cone geometry as Phoenix.[28]
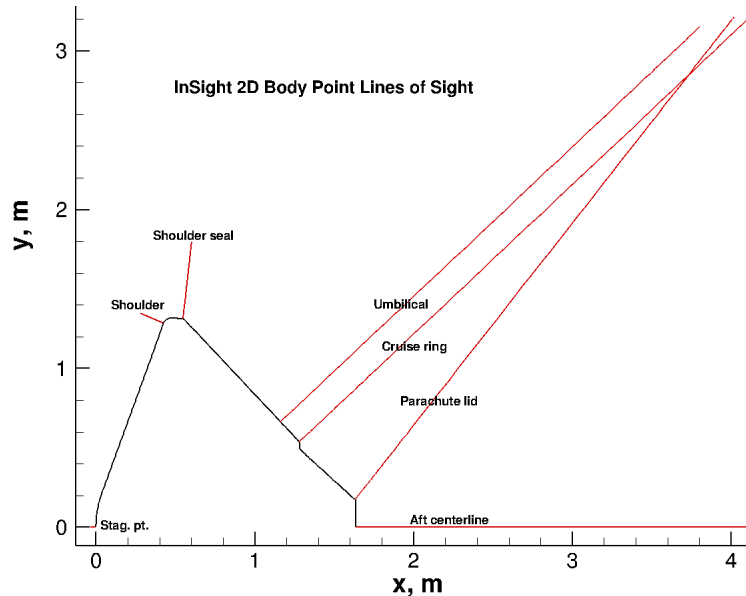

Figure 5. 2-D cross-section of InSight detailing normal lines of sight evaluated with NEQAIR.

This section presents fore-body and after-body heating results corresponding to a proposed maximum fore-body heating trajectory for the InSight vehicle. DPLR and NEQAIR have been used to estimate the convective and radiative heating for the body point locations shown in Fig. 5. The results of these calculations are presented in Fig. 6. Note that for these calculations, NEQAIR was run in tangent slab mode on axisymmetric flow solutions, both of these assumptions will be shown to be questionable for wake flows in the next section. This has been the traditional practice now being reconsidered in this work. Figures 6(a) and 6(b) show that at the fore-body locations (stagnation point and shoulder), convective heating is almost completely dominant. On the after-body, however, several of the locations show the radiative heating to be at a similar magnitude to the convective heating (Figs. 6(c) and 6(e)), while in the case of the umbilical location, radiative heating is the dominant mechanism (Fig. 6(d)). Even though the heating values are substantially smaller on the after-body, the magnitude is important as the TPS on the after-body is designed to handle a much smaller load than the fore-body. Additionally, the radiative heat flux peaks later in the trajectory than convection. This is explained by the higher density of CO_2 present at the lower temperatures encountered later in the trajectory. Figure 7 shows the impact of the tangent slab approximation versus full angular integration as predicted by LAURA/HARA over the vehicle surface at one point in the trajectory. The tangent slab over-prediction is substantial, between 25% - 30% on average and is particularly large at sharp corners, such as the cruise ring step or parachute lid. This phenomenon will be discussed in more detail in the next section.
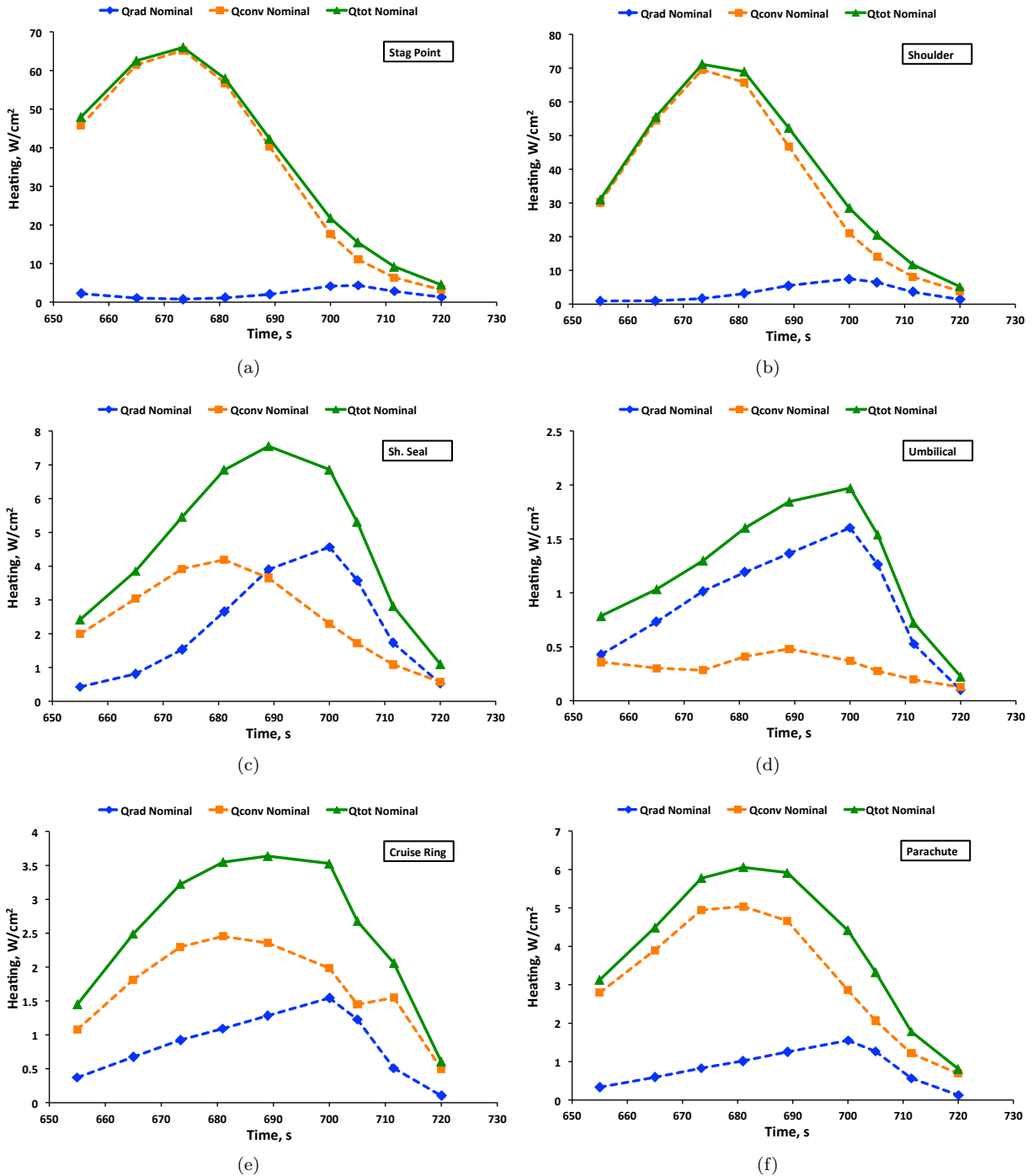
American Institute of Aeronautics and Astronautics

Figure 6. Convective and radiative heating axisymmetric/tangent slab calculations by DPLR/NEQAIR for various locations on the InSight geometry.
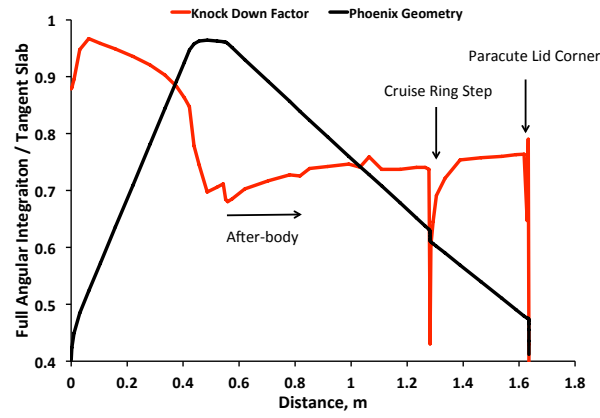
American Institute of Aeronautics and Astronautics

Figure 7. Ratio of full angular integration vs tangent slab for Phoenix geometry calculated with LAURA/HARA.

IV.B.   MSL Geometry

This section presents radiative heating results for the MSL geometry (which will also be used by NASA for the upcoming Mars 2020 mission) for two different trajectory points on the peak 3-sigma convective heat load trajectory.[29] Figures 8 and 9 show the shock and wake temperature contours for 71.5 s and 87.5 s as calculated by DPLR and LAURA respectively. The DPLR and LAURA flow-fields show qualitative agreement for the dominant flow structure. The 71.5 s point corresponds to peak convective heating on the fore-body. A tangent slab calculation at two points (labeled 1 and 3) on the back-shell had previously identified 87.5 s as the peak radiative flux on the back-shell. Various interactions of expanding shocks can be observed in the instantaneous center-line slices of the unsteady 3-D wakes, creating complex flow-fields. The hot and cold spots in the wake change in both position and magnitude throughout the trajectory. Given this variability, the actual time of peak back-shell heating may differ were the entire trajectory to be evaluated using full angular integration. However, this task would be computationally intensive and was not attempted here. The figure also shows the locations of the various body points (co-ordinates detailed in Table 1) used in this analysis and the locations of the normal lines of sight from these points. This section will provide the results of the radiative heat flux calculations for these points as well as detailing the convergence of the calculations as functions of both the extent of the CFD grid into the wake and the number of hemisphere lines of sight used in full angular integration.
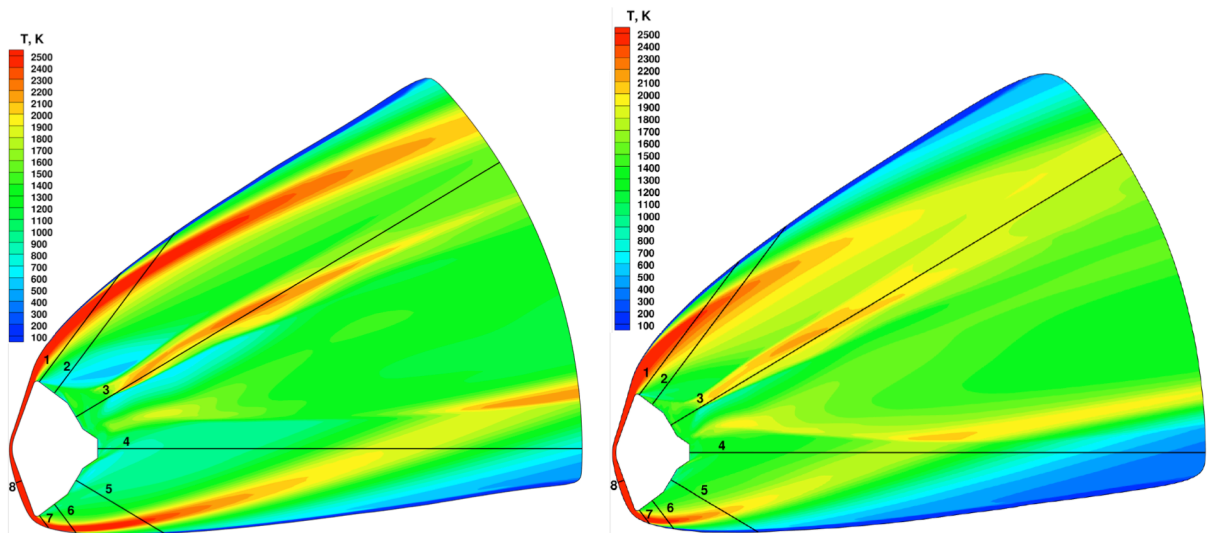
(a) V = 5259 m/s, ρ = 8.22e-4 kg/m^3, T = 176 K, α = 17.1°   (b) V = 3624 m/s, ρ = 2.06e-3 kg/m^3, T = 198 K, α = 17.5°

Figure 8. DPLR results for flow-field temperature of an MSL pre-flight design trajectory at (a) 71.5 s and (b) 87.5 s.

American Institute of Aeronautics and Astronautics
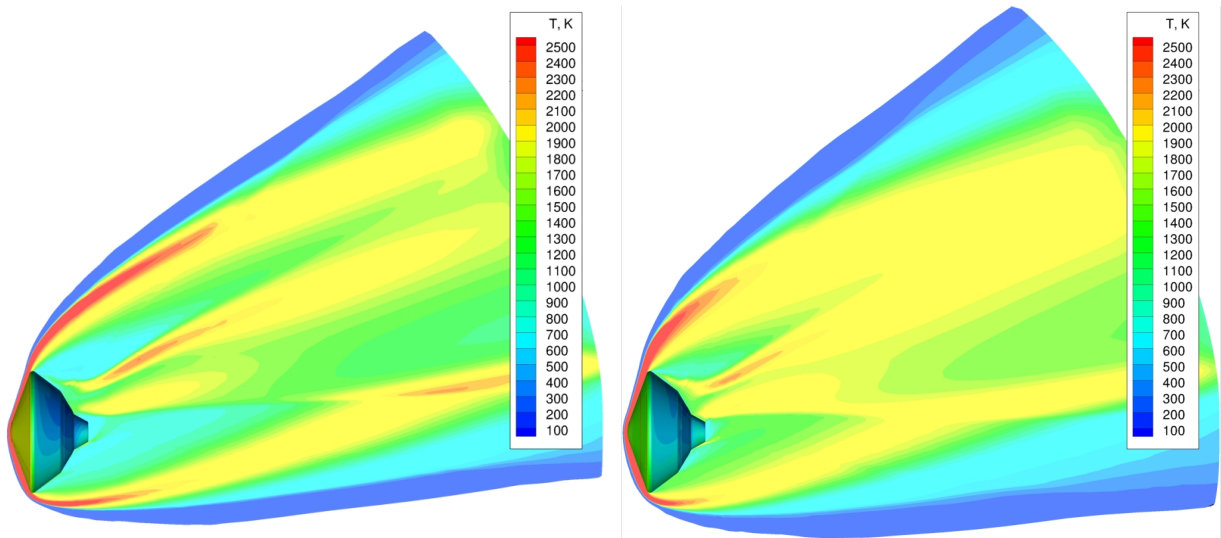
(a) V = 5259 m/s, ρ = 8.22e-4 kg/m^3, T = 176 K, α = 17.1° (b) V = 3624 m/s, ρ = 2.06e-3 kg/m^3, T = 198 K, α = 17.5°

Figure 9. LAURA results for flow-field temperature of an MSL pre-flight design trajectory at (a) 71.5 s and (b) 87.5 s.

Table 1. Co-ordinates for body point locations used in calculations for MSL geometry

Number	Name	x	y	z
		Origin: Vehicle Nose		
1	Aft Seal, Leeside	0.89863	0	2.223282
2	Mid-Cone 1, Leeside	1.40096	0	1.84612
3	Mid-Cone 2, Leeside	2.11729	0	1.05282
4	Parachute Closeout Cone	2.84241	0	0
5	Mid-Cone 2, Windside	2.11729	0	-1.05282
6	Mid-Cone 1, Windside	1.40096	0	-1.84612
7	Aft Seal, Windside	0.89863	0	-2.223282
8	Stagnation Point	0.316756	0	-1.06864

American Institute of Aeronautics and Astronautics

IV.B.1. Length of the Wake

This section will determine the impact of how far the CFD grid is extended into the wake has on radiative heating. Figures 10(a) and 10(b) show that at t = 87.5 s, DPLR and LAURA show quite good agreement for T, T_v and the number densities of CO_2 and CO for the normal line of sight from body point 2. However, when the line of sight is compared for body point 3, as shown in Fig. 10(c) and 10(d), even though the magnitude is roughly consistent between the two codes, the spatial variation is not matched well due to the different reaction rates implemented. Figures 10(c) and 10(d) also show that, even after extending the flow 20 m in the wake (which corresponds to 5.07 D), the temperature of the flow is still near 2000 K, where CO_2 will still radiate significantly in the mid-infrared. Figure 11(a) shows how the tangent slab radiative heat flux to the vehicle surface is converging as the length of the wake evaluated is increased. The radiance is still not completely converged by 20 m, as the radiative heat flux still changed by 3% compared to the value at 18 m. Figure 11(b) shows where the radiative heat flux imparted on the back-shell is originating from in the wake for body point 3 using tangent slab. The plot shows that the radiation is steadily increasing from 20 m to 8 m, then begins to plateau, and finally, a small amount of absorption occurs close to the body. The linear dependence near the edge of the domain indicates that the radiance is fairly constant despite the decreasing CO_2 concentration. The plateau at 8 m indicates that the radiation is becoming optically thick and this is responsible for the convergence observed in Fig. 11(a). However, as the tangent slab is based on only a single line of sight, this result does not capture the decreasing solid angle at long distances, nor does it account for the off-normal flow structure in the wake.
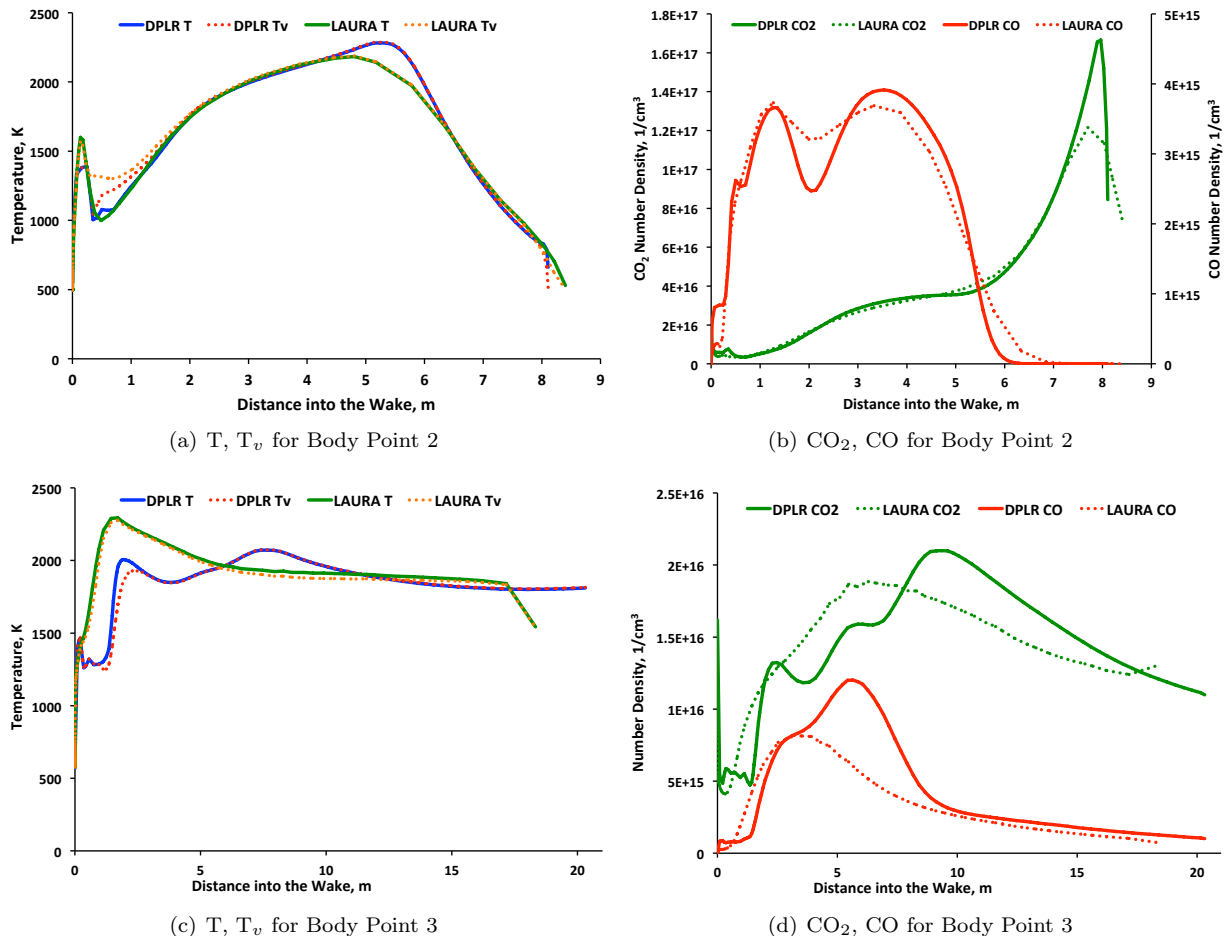

(a) T, T_v for Body Point 2

(b) CO_2, CO for Body Point 2

(c) T, T_v for Body Point 3

(d) CO_2, CO for Body Point 3

Figure 10. Comparison of DPLR and LAURA flow-fields for t = 87.5 s.

American Institute of Aeronautics and Astronautics
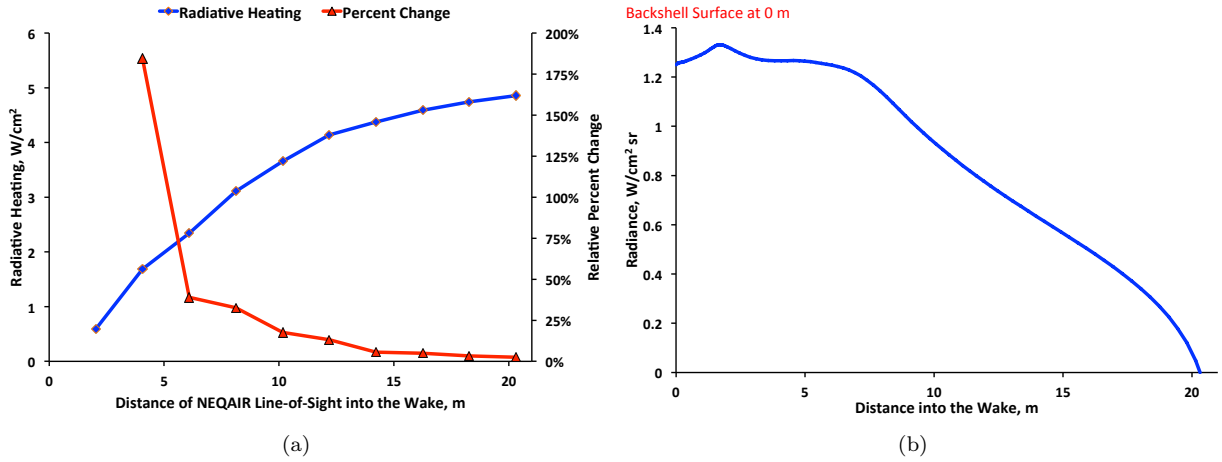
(a)   (b)

Figure 11. Convergence of tangent slab radiance as a function of distance into the wake of the DPLR solution for Body Point 3, t = 87.5 s.

Comparisons of the tangent slab and full angular integration calculations for two wake lengths are given in Table 2. The full angular integration calculations were performed with the higher (1122 line) resolution. The results show that most body points have radiative heat fluxes of several watts per square centimeter, and can be as high as 6.7 W/cm^2 or 5.2 W/cm^2 when calculated by tangent slab or full angular integration, respectively. Only points 3 and 4 show significant variation with the length of the wake simulated. All the other body points cross the shock and reach free-stream conditions regardless of the wake length included, and so do not depend upon how far the CFD grid is extended into the wake. The normal lines of sight from points 3 and 4, however, remain in the wake their entire length so they display significant sensitivity to wake length. The full angular integration, however, accounts for the solid angle subtended by the wake boundary and is therefore less sensitive to wake length. In this case the degree of convergence is reduced from around 40% to 10%. Body point 3 was further analyzed with three different grid sizes at the t=71.5 s point, as shown in Table 3. These results indicate that a wake distance of approximately 4 diameters is required to capture the radiation emitted onto the back-shell using 3-D integration.

Table 2. t = 87.5 s. Short Wake Grid is 2.23 D and Long Wake Grid is 5.07 D

Radiative Heating, W/cm^2							
	Tangent Slab (TS)			**Full Angular Integration (FA)**			
			Percent			Percent	Percent
Line of	Short Wake	Long Wake	Difference	Short Wake	Long Wake	Difference	Difference
Sight	2.23 D (s)	5.07 D (l)	(TS$_l$ - TS$_s$)/TS$_l$	2.23 D (s)	5.07 D (l)	(FA$_l$ - FA$_s$)/FA$_l$	(TS$_l$ - FA$_l$)/TS$_l$
1	6.705	6.710	0.075%	5.016	5.190	3.4%	23%
2	4.479	4.582	2.3%	3.360	3.559	5.6%	22%
3	2.772	4.852	42.9%	1.803	2.021	10.8%	58%
4	0.754	1.140	33.9%	1.034	1.224	15.5%	-7.4%
5	1.353	1.388	2.5%	1.208	1.279	5.6%	7.9%
6	2.555	2.540	-0.59%	2.134	2.143	0.42%	16%
7	5.081	5.073	-0.16%	3.773	3.782	0.24%	25%
8	10.018	10.086	0.67%	9.521	9.562	0.43%	5.2%

Table 3. t = 71.5 s, BP 3

Radiative Heating, W/cm^2					
Length of Wake	Tangent slab (TS)	Convergence Difference	Full Angular Integration (FA)	Convergence Difference	Method Difference
2.28 x D	1.73	–	1.18	–	31.8%
4.21 x D	2.29	24.5%	1.43	17.5%	37.6%
4.93 x D	2.38	3.8%	1.45	1.4%	39.1%

IV.B.2.   Tangent Slab vs. Full Angular Integration

Typically, radiative heat flux is calculated using a tangent slab method due to its ease of implementation, quickness and accuracy for locations of dominant heating, such as the stagnation point. However, as this section will show, the tangent slab method does not provide good results in calculating back-shell radiation. The tangent slab is inaccurate for after-body calculations due to the complexity of the wake flow. This is highlighted in Fig. 12 which shows the radiant intensity (i.e., body normal component of radiance) contour plotted on the triangulated surface formed by the intersections of the hemisphere lines of sight with the outer grid boundary, for the 8 body points. The origin of each plot corresponds to the body-normal line which is the basis for the tangent slab calculation. The full angular heat flux is equivalently calculated by integrating over the area of the projection plot with respect to solid angle, while tangent slab contours would appear circularly symmetric on this plot. It is evident from the non-uniform and non-symmetrical structure of the radiance shown in figures 12(a) to 12(j) that the tangent slab approximation is not valid. Figures 12(k) and 12(l) show an example of a body point location where tangent slab should be relatively accurate (the stagnation point), as the radiance is symmetric and centered on the origin. Comparing each body point pair at the two trajectory times of 71.5 and 87.5 s, it is apparent that the angular dependence of the radiance is quite different (e.g., Figs. 12(a) to 12(f)) and in some cases the location of the peak radiance has shifted (Figs. 12(g) and 12(j)). This indicates that a constant tangent slab knock-down factor cannot generally be applied over an entire trajectory.

Results from tangent slab calculations using normal lines of sight from each body point, and the full angular integration calculations are given in Table 4. The full angular integration calculations were performed with two resolution settings for all body points to give an indication of convergence, one using 306 lines to define half the hemisphere, and the other using 1122 lines. The CFD grid was extended 5.07 x D (where D is the vehicle diameter) into the wake. The results show that most body points show radiative heat flux of several watts per square centimeter, and can be as high as 5.83 W/cm^2 or 3.26 W/cm^2 when calculated by tangent slab or full angular integration, respectively. Only points 4 (aft symmetry point) and 8 (stagnation line) show consistent results between tangent slab and full angular integration. For the stagnation point, the tangent slab method over-predicts the full angular integration value by 7.1%, which is consistent with the expected over-prediction of within 10%. Point 4, looking directly into the wake from the base of the vehicle, presents a nearly symmetrical geometry and as such is well estimated by tangent slab. Though the tangent slab approximation is within 10% of the full angular integration, in this case it is actually an under-prediction of the heat flux. This is because the wake is colder on the normal line of sight than it is off angle. This makes the point that it is not necessarily safe to assume that tangent slab will always be conservative. Body points 1, 2, 3, 6 and 7 all show a reduction of approximately 40% for full angular integration compared to tangent slab while body point 5 shows a reduction of 23%. These knock downs are significant; for example, this corresponds to a reduction of approximately 2.6 W/cm^2 at body point 1.
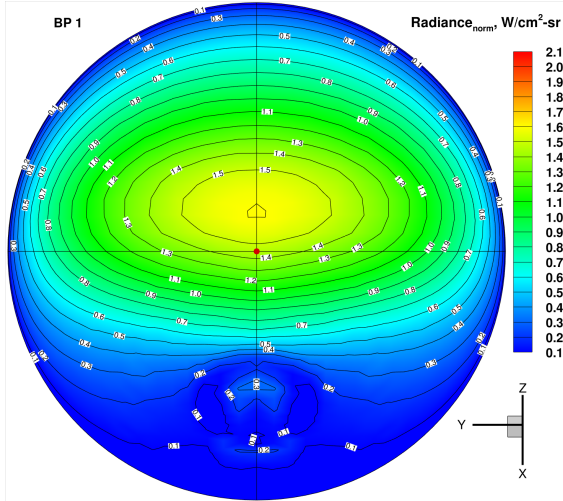
Table 4 also shows the results from the two different resolutions used in the full angular integration calculations. All body points except for 1 and 6 are within 4% when the results with the two different resolutions are compared, suggesting they have been reasonably well converged. For these cases, the lower resolution value is always larger than high resolution, even when the tangent slab approximation is not. This means that the coarse grid will usually be a conservative estimate. However, it is still possible that sufficiently complicated wake structures may produce an exception to this. Without further full angular integration calculations at lower, medium or finer resolutions, it is not clear from this table whether body points 1 and 6 have converged. As body point 6 shows the worst level of convergence, two extra resolutions were run using 90 and 650 lines, as shown in Fig. 13. This figure suggests that a convergence of less than

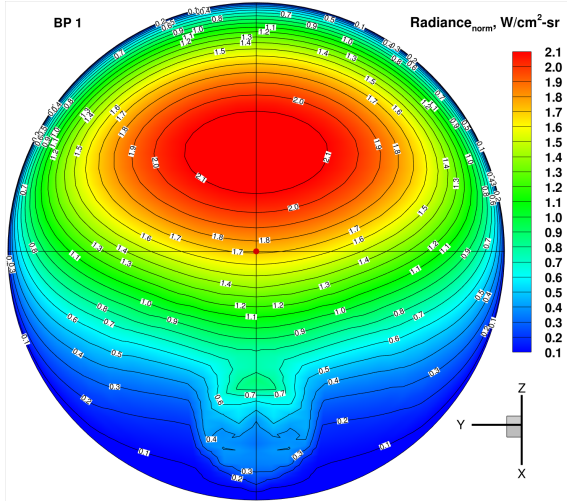1% is achieved if more than 600 hemisphere lines of sight are used.

The convergence of the triangulation itself is determined by evaluating the solid angle calculated based on the selected points and comparing it to 2π. For the lower resolution of 306 lines, all body points are generally within 5% of predicting half a hemisphere, while the 1122 line grid shows that the body points are within 1.4%. While these values are suggestive of the accuracy of the integration calculation, the values in Table 4 show that they are neither an upper nor a lower bound to convergence. The previously stated conclusion that a constant tangent slab to full angular integration knock down factor is not possible is also verified with the results presented in this table. For 71.5 s, the knock down factor is on average approximately 40%. While for the results presented in Table 2, the knock down factor was on average approximately 25%, with body point 3 at 58%. A constant factor would be beneficial in the sense that calculations could be run using the significantly more time-efficient tangent slab method, then compensated for with the difference from full angular integration by a knock-down factor. However, as this is not appropriate, the full angular integration method would need to be applied across the entire trajectory to provide an accurate calculation for total heat load at any given body point.

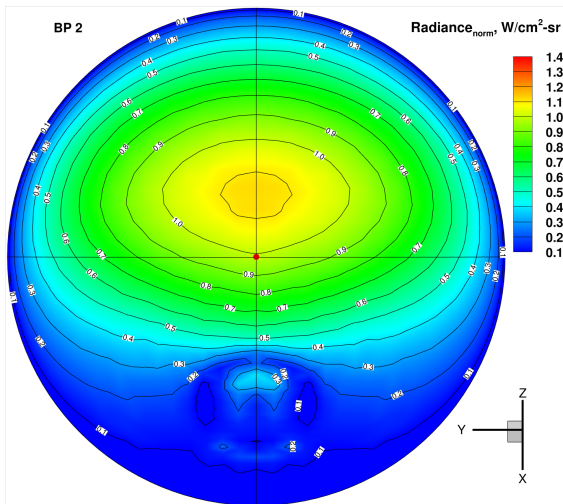Table 4. Comparison of Tangent Slab and Full Angular Integration methods at t = 71.5 s

	Radiative Heating, W/cm^2			Percent Difference	
Body Point	Tangent Slab (TS)	Full Angular Integration: coarse (FA$_c$) [Res. 306]	Full Angular Integration: fine (FA$_f$) [Res. 1122]	Tangent Slab Accuracy (TS - FA$_f$)/TS	Coarse vs Fine Full Angular Integration (FA$_f$ - FA$_c$)/FA$_f$
1	5.83	3.46	3.26	44%	-6.1%
2	4.07	2.51	2.44	40%	-2.9%
3	2.2	1.443	1.43	35%	-0.9%
4	0.8	0.884	0.879	-9.9%	-0.6%
5	1.28	1.002	0.998	23%	-1.4%
6	2.24	1.57	1.44	36%	-9.0%
7	3.22	1.99	1.92	40%	-3.6%
8	2.96	2.78	2.75	7.1%	-1.1%

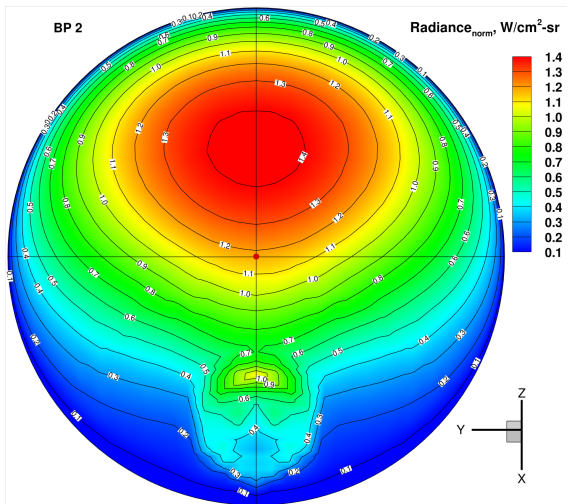American Institute of Aeronautics and Astronautics

(a) 71.5 s / BP 1

(b) 87.5 s / BP 1

(c) 71.5 s / BP 2

(d) 87.5 s / BP 2

(e) 71.5 s / BP 3

(f) 87.5 s / BP 3

American Institute of Aeronautics and Astronautics
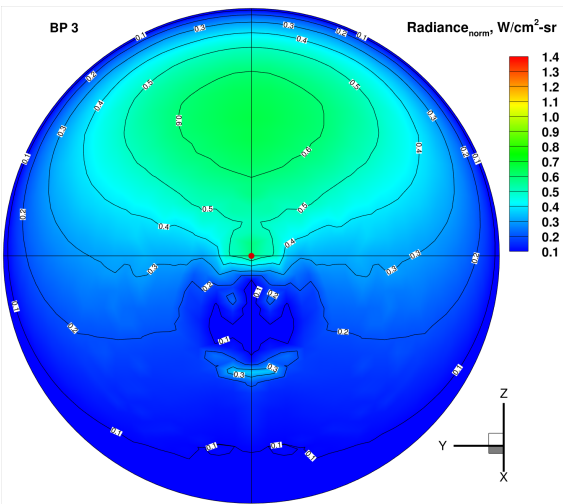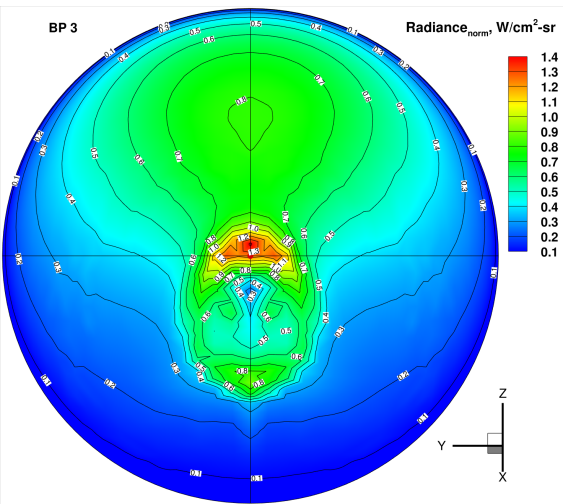
(g) 71.5 s / BP 6

(h) 87.5 s / BP 6

(i) 71.5 s / BP 7

(j) 87.5 s / BP 7

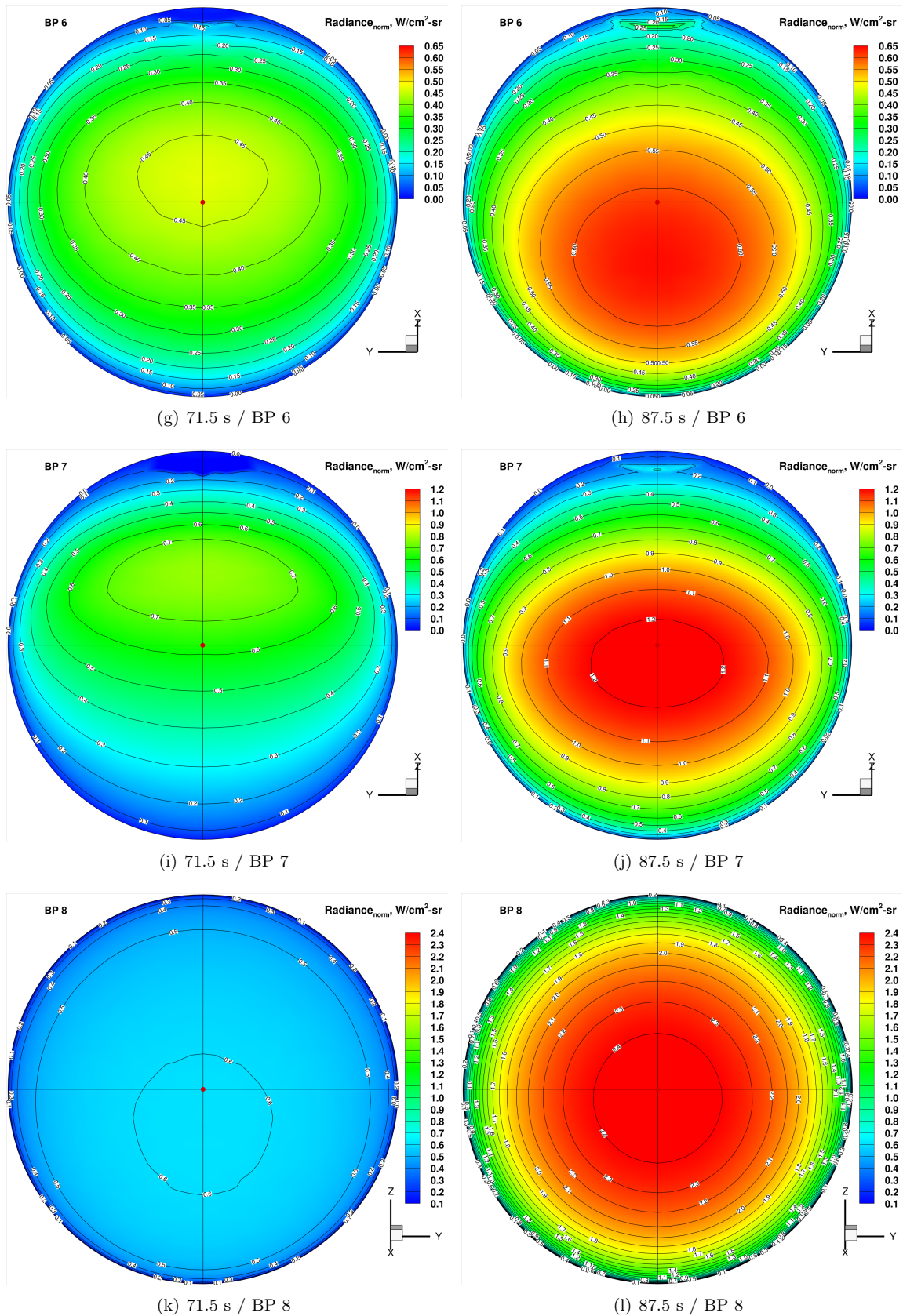(k) 71.5 s / BP 8

(l) 87.5 s / BP 8

Figure 12. Surface projected radiance for various body point locations at 71.5 s and 87.5 s.
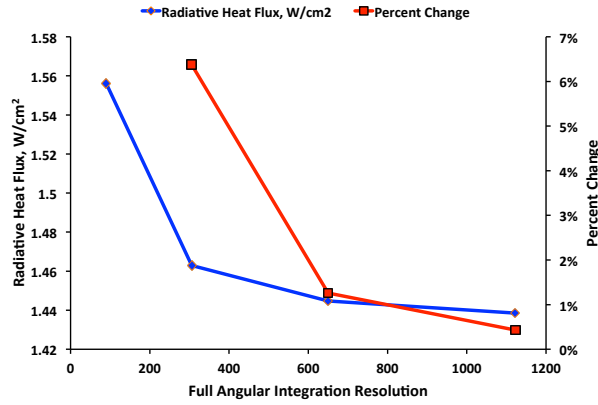
Figure 13. Convergence of radiative heat flux as a function of number of lines of sight for body point 6 at 71.5 s.

V.   Summary of Results and Code Comparison

This section provides a summary of the heating magnitudes of interest for the InSight trajectory as well as the final converged radiative heating for the MSL geometry at both trajectory times analyzed in this paper. Table 5 details the peak convective and radiative heat flux as well as the convective and radiative components of the total heat load for the Phoenix/InSight geometry. The table summarizes how convective heating is clearly dominant on the fore-body, while the radiation component can be approximately equal to convective heat flux on the after-body (Shoulder Seal and Aft Centerline) and even dominant (Umbilical location). However, it should be noted that these radiative heating values were calculated with tangent slab, which has now been shown here to provide an over-prediction compared to the full angular integration method. For a more accurate representation of the impact of radiative heating, full angular integration calculations are required. This paper has also highlighted that the tangent slab values cannot be scaled by a knock-down factor to approximate full angular integration results.

Table 5.   NEQAIR Peak Convective and Radiation for Phoenix geometry

	Body Point	Peak Convective, W/cm^2	Peak Radiative (Tangent Slab), W/cm^2	Convective Heat Load, J/cm^2	Radiative Heat Load (Tangent Slab), J/cm^2
Fore-body	Stag. Pt.	65.2	4.36	2408	140
	Shoulder	69.5	7.50	2491	234
After-body	Shoulder Seal	4.2	4.56	176	152
	Umbilical	0.48	1.60	21	64
	Cruise Ring	2.45	1.54	120	60
	Parachute	5.04	1.55	220	58
	Aft Centerline	5.21	4.49	204	184

Tables 6 and 7 show the final converged radiative heating values for MSL calculated with NEQAIR based on DPLR flow-fields. The table also shows code-to-code comparisons against results obtained with HARA based on LAURA flow-fields for both tangent slab and full angular integration. Laminar convective heating values calculated by LAURA are also provided to give an indication of the significance for radiative heating to the total heat flux. The table shows that excellent agreement is obtained between both sets of codes when full angular integration is used, with the radiative heating at both times for all body points being within 14% (in general, the difference is much less). However, the agreement when the tangent slab method is used is significantly worse (difference as high as 33.4% for body point 4 at t = 71.5 s). This is due to the differences in the flow-fields along the normal line of sight and also the manner in which the normal line of sight is selected. Small differences in this methodology (such as the exact location of the body point used to extract the normal line) when applied to a complicated wake structure, as shown in Figs. 12(c) - 12(f), can make a large difference in the tangent slab value. Differences along individual lines of sight become averaged out once the entire flow-field is considered, however, leading to more consistent full angular integrations. Tables 6 and 7 also show that radiative heating is significantly higher than the laminar convective heating

American Institute of Aeronautics and Astronautics

value for body points 1 through 6, and therefore highlights its importance in the design of after-body TPS.

Table 6. Comparing NEQAIR and HARA for MSL Geometry at t = 71.5 s

Body Point	Full Angular Integration Radiative Heating, W/cm^2		Percent Difference	Tangent Slab Radiative Heating, W/cm^2		Percent Difference	Laminar Convective Heating, W/cm^2
	NEQAIR	HARA		NEQAIR	HARA		LAURA
1	3.26	3.24	-0.62%	5.83	6.25	-7.2%	0.86
2	2.44	2.39	2.0%	4.07	4.06	0.2%	0.09
3	1.43	1.52	-6.3%	2.2	2.13	3.2%	0.46
4	0.88	0.973	-10.6%	0.8	1.07	-33.4%	0.17
5	1.00	1.06	-6.0%	1.28	1.43	-11.7%	0.40
6	1.44	1.45	-0.7%	2.24	2.22	0.9%	1.90
7	1.92	1.83	4.7%	3.22	2.68	16.8%	12.15
8	2.75	2.55	7.3%	2.96	2.75	7.1%	51.35

Table 7. Comparing NEQAIR and HARA for MSL Geometry at t = 87.5 s

Body Point	Full Angular Integration Radiative Heating, W/cm^2		Percent Difference	Tangent Slab Radiative Heating, W/cm^2		Percent Difference	Laminar Convective Heating, W/cm^2
	NEQAIR	HARA		NEQAIR	HARA		LAURA
1	5.19	5.23	-0.8%	6.71	7.29	-8.6%	0.74
2	3.56	3.57	-0.4%	4.58	4.60	-0.4%	0.18
3	2.02	2.14	-6.0%	4.85	5.73	-18.0%	0.26
4	1.22	1.39	-13.9%	1.14	1.46	-28.4%	0.08
5	1.28	1.39	-8.6%	1.39	1.60	-14.9%	0.46
6	2.14	2.23	-3.9%	2.54	2.72	-7.0%	1.97
7	3.78	3.93	-4.0%	5.07	5.4	-6.2%	4.38
8	9.56	9.12	4.6%	10.09	10.02	0.7%	21.7

VI.   Conclusion

The paper has highlighted back-shell radiation predictions for planned and actual Mars entry geometries in terms of the two main radiation flow-field codes, DPLR/NEQAIR and LAURA/HARA, which are used at NASA Ames and Langley, respectively. Detailed heating results are given for both the upcoming Mars Insight flight and the recent MSL entry. In the code comparison, it was first shown that the CO_2 radiation predictions within NEQAIR and HARA agreed within 2% when the flow-field input was identical. Next, full angular integrations conducted were shown to have excellent agreement, with the radiative heating calculated at all body points with both sets of codes agreeing within 14%, and in general, the agreement is much better. The convergence of the full angular integration was analyzed with respect to the length that the CFD grid is extended into the wake and the number of angular points / lines of sight used in the full angular integration. For the MSL case, a wake distance of approximately 4 D and greater than 600 angular points were estimated to converge the results within 5%. The variation obtained with tangent slab evaluations showed significantly greater difference between the two codes, up to 33.4%. Several of the analyses presented in this paper have shown that tangent slab does not provide an accurate indication of after-body heating, and cannot be scaled in a general way to approximate the more rigorous full angular integration result.

Even though the absolute values of the after-body heating are relatively small compared to the fore-body, the total heat flux can be significant compared to what the back-shell TPS material is designed to withstand. The total heat flux used for design is further increased due to the traditionally large uncertainty on back-shell calculations. Therefore, it is clear that understanding after-body heating is important for TPS design. This is particularly vexing for upcoming missions like InSight and Mars 2020, as they are built-to-print missions

of Phoenix and MSL, respectively, and neither mission considered radiative heating in the original design. By including after-body radiative heating with appropriate uncertainty, there is potential that the margined heating value would exceed the build-to-print design. The results presented in this paper show that radiative heating is significant for both the MSL and Phoenix geometry, and therefore also needs to be considered for any future Mars mission. Furthermore, the results show that after-body radiative heating can be larger than convective heating, and could lead to an un-margined total heat flux on the after-body up to 14 W/cm^2.

Acknowledgments

References

[1]Tashkun, S. and Perevalov, V., "CDSD-4000: High-Resolution, High-Temperature Carbon Dioxide Spectroscopic Databank," *Journal of Quantitative Spectroscopy and Radiative Transfer*, Vol. 112, No. 9, 2011, pp. 1403–1410.

[2]Babou, Y., Riviere, P., Perrin, M.-Y., and Soufiani, A., "Spectroscopic data for the prediction of radiative transfer in CO_2-N_2 plasmas," *Journal of Quantitative Spectroscopy and Radiative Transfer*, Vol. 110, No. 1-2, 2009, pp. 89 – 108.

[3]da Silva, M. L. and Beck, J., "Contribution of CO_2 IR Radiation to Martian Entries Radiative Wall Fluxes," *Proceedings of the 49th AIAA Aerospace Sciences Meeting and Exhibition, 2011*, Proceedings of the 49th AIAA Aerospace Sciences Meeting and Exhibition, 2011, AIAA, 2005. AIAA 2011-135.

[4]LeBrun, A. and Omaly, P., "Investigation of Radiative Heat Fluxes for EXOMARS Entry in the Martian Atmosphere," *Proceedings of the 4th International Workshop on Radiation of High Temperature Gases in Atmospheric Entry*, 2010.

[5]Palmer, G. and Cruden, B., "Experimental Validation of CO_2 Radiation Simulations," *43rd AIAA Thermophysics Conference*, New Orleans, Louisiana, 2012, AIAA 2012-3188.

[6]Mazaheri, A., Johnston, C., and Sefidbakht, S., "Three-Dimensional Radiation Ray Tracing for Shock-Layer Radiative Heating Simulations," *Journal of Spacecraft and Rockets*, Vol. 50, No. 3, 2013, pp. 485–493.

[7]Cruden, B., Prabhu, D., and Brandis, A., "Measurement and Characterization of Mid-wave Infrared Radiation CO_2 Shocks," *11th AIAA/ASME Joint Thermophysics and Heat Transfer Conference*, Atlanta, Georgia, 2014, AIAA 2014-2962.

[8]Cozmuta, I., Wright, M., Laub, B., and Wilcoxson, W., "Defining Ablative Thermal Protection System Margins for Planetary Entry Vehicles," *42nd AIAA Thermophysics Conference*, Honolulu, HI, 2011, AIAA-2011-3757.

[9]Johnston, C. and Brandis, A., "Features of Afterbody Radiative Heating for Earth Entry," *Journal of Spacecraft and Rockets*, Vol. 52, No. 1, 2015, pp. 105–119.

[10]Mazaheri, A., Gnoffo, P., Johnston, C., and Kleb, B., "LAURA Users Manual," Tech. Rep. NASA TM 2010-216836, 2010.

[11]Gnoffo, P., Gupta, R., and Shinn, J., "Conservation equations and physical models for hypersonic air flows in thermal and chemical nonequilibrium," Tech. Rep. NASA TP-2867, 1989.

[12]Roe, P., "Approximate Riemann Solvers, Parameter Vectors, and Difference Schemes," *Journal of Computational Physics*, Vol. 43, No. 2, 1981, pp. 357–372.

[13]Yee, H., "On Symmetric and Upwind TVD Schemes," Tech. Rep. NASA TM-88325, 1986.

[14]Wright, M., *A Family of Data-Parallel Relaxation Methods for the Navier-Stokes Equations*, Ph.D. thesis, University of Minnesota, 1997.

[15]Wright, M., Candler, G., and Bose, D., "Data-Parallel Line Relaxation Method for the Navier-Stokes Equations," *AIAA Journal*, Vol. 36, No. 9, 1998, pp. 1603–1609.

[16]Wright, M., White, T., and Mangini, N., "Data-Parallel Line Relaxation (DPLR) Code User Manual Acadia-Version 4.01.1," NASA/TM-2009-215388, NASA Ames Research Center, October 2009.

[17]Johnston, C., Hollis, B., and Sutton, K., "Spectrum Modeling for Air Shock-Layer Radiation at Lunar-Return Conditions," *Journal of Spacecraft and Rockets*, Vol. 45, No. 5, 2008, pp. 865–878.

[18]Johnston, C. O., Hollis, B., and Sutton, K., "Non-Boltzmann Modeling for Air Shock Layers at Lunar Return Conditions," *Journal of Spacecraft and Rockets*, Sep.-Oct. 2008.

[19]Ralchenko, Y., "NIST Atomic Spectra Database, Version 3.1.0," physics.nist.gov/PhysRefData/ASD/, July 2006, last accessed September 3rd, 2007.

[20]The Opacity Project Team, *The Opacity Project*, Vol. 1, Bristol and Philadelphia: Institute of Physics Publishing, 1995.

[21]Cunto, W., Mendoza, C., Ochsenbein, F., and Zeippen, C., "TOPbase at the CDS," *Astronomy and Astrophysics*, Vol. 275, Aug. 1993, pp. L5–L8, see also http://cdsweb.u-strasbg.fr/topbase/topbase.html.

[22]Whiting, E., Park, C., Yen, L., Arnold, J., and Paterson, J., "NEQAIR96, Nonequilibrium and Equilibrium Radiative Transport and Spectra Program: User's Manual," Technical Report NASA RP-1389, Ames Research Center, Moffett Field, Moffett Field, 1996.

[23]Kramida, A., Ralchenko, Y., Reader, J., and Team, N. A., "NIST Atomic Spectra Database, Version 5.0.0," physics.nist.gov/asd/, July 2012, last accessed July, 2012.

[24]Cruden, B. and Brandis, A., "Updates to the NEQAIR Radiation Solver," St. Andrews, Scotland, November 2014.

[25]Johnston, C. and Brandis, A., "Modeling of nonequilibrium CO Fourth-Ppositive and CN Vinlet emission in $CO_2 - N_2$ gases," *Journal of Quantitative Spectroscopy and Radiative Transfer*, Vol. 149, 2014, pp. 303–317.

[26]Saunders, D. and White, T., "CFD Utilities <http://sourceforge.net/projects/cfdutilities/files/adt/>," 2015.

[27]Edquist, K., Desai, P., and Schoenenberger, M., "Aerodynamics of Mars Phoenix Entry Capsule," *Journal of Spacecraft and Rockets*, Vol. 48, No. 5, 2011, pp. 713–726.

[28]Asmar, S., Oudrhiri, K., Kurtik, S., and Weinstein-Weiss, S., "Communications During Critical Mission Operations: Preparing for InSight's Landing on Mars," *SpaceOps Conferences*, Pasadena, CA, 2014, AIAA 2014-1713.

[29]Edquist, K., Dyakonov, A., Wright, M., and Tang, C., "Aerothermodynamic Design of the Mars Science Laboratory Backshell and Parachute Cone," *41st AIAA Thermophysics Conference*, San Antonio, Texas, 2009, AIAA 2009-4078.

American Institute of Aeronautics and Astronautics